Journal of Power Sources 601 (2024) 234287

Contents lists available at ScienceDirect

Journal of Power Sources

journal homepage: www.elsevier.com/locate/jpowsour

Flexible inkjet-printed lithium-ion batteries with $Ti_3C_2T_x$ current collector

Prisca Viviani [a], Eugenio Gibertini [a], Paolo Fontana [a], Federico Lissandrello [a], Yury Gogotsi [b], Luca Magagnin [a,*]

[a] Dipartimento di Chimica, Materiali e Ingegneria Chimica "Giulio Natta", Politecnico di Milano, Via Luigi Mancinelli 7, 20131, Milan, Italy
[b] A.J. Drexel Nanomaterials Institute and Department of Materials Science and Engineering, Drexel University, 3141 Chestnut Street, Philadelphia, PA, 19104, United States

HIGHLIGHTS

- Aqueous-based ink formulations were presented.
- $Ti_3C_2T_x$ current collector adopted for the first time in an inkjet printed full cell.
- LTO/LFP cell with $Ti_3C_2T_x$ was tested under bending with no performances losses.
- $Ti_3C_2T_x$ proved an improvement of the gravimetric energy density of 21% compared.

GRAPHICAL ABSTRACT

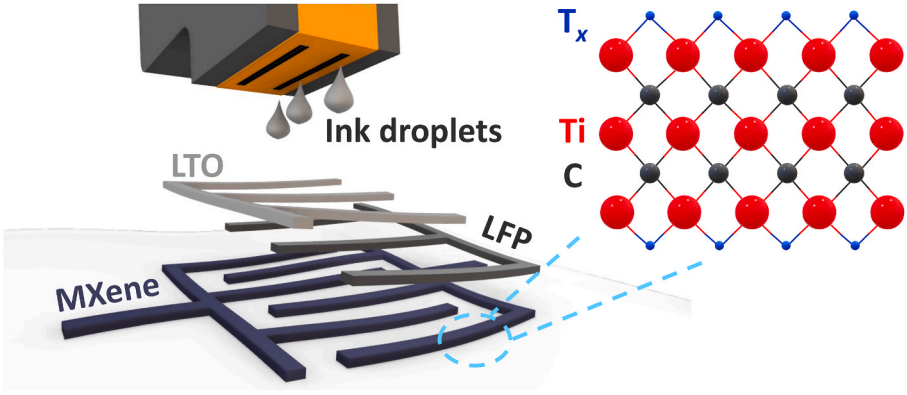

ARTICLE INFO

Keywords:
MXenes
Inkjet printing
Flexible lithium-ion battery
Current collector

ABSTRACT

The Internet of Things (IoT) market is a quickly growing field that has great economic potential and attracts interest from researchers. Progress in this field relies on the ability to integrate smart devices with everyday objects and instruments. Therefore, energy storage plays a critical role in powering these devices. In this context, inkjet printing of batteries can be framed as a potentially innovative fabrication technique that combines the benefits of thin-film technology for lightness, mechanical flexibility, and ease of integration. The main bottleneck to obtaining a full inkjet-printed battery is printing the current collector (CC), whose role is to electrically bridge the electrodes to an external circuit and mechanically support the electrodes. A simple ink formulation based on hydrophilic and electronically conductive $Ti_3C_2T_x$ MXene has been proposed for printing current collectors in this work. We have analyzed substrate compatibility and the necessity of the adopted device configurations. Also, a fully printed battery with good flexibility has been produced and showed no performance degradation upon bending. The results of this study show that $Ti_3C_2T_x$ MXene is a promising candidate for flexible printed current collectors. However, an improvement in the electrochemical performance, in particular the areal capacity of the device, is still necessary for practical use. This may be achieved by minimizing the spacing between the electrodes using a printer with a higher resolution.

* Corresponding author.
E-mail address: luca.magagnin@polimi.it (L. Magagnin).

https://doi.org/10.1016/j.jpowsour.2024.234287
Received 23 December 2023; Received in revised form 9 February 2024; Accepted 28 February 2024
Available online 8 March 2024

1. Introduction

The rise of flexible/wearable electronics requires the integration of flexible energy storage devices to power smart devices that can collect and communicate data independently [1,2]. One of the major limitations of conventional batteries is their rigidity and poor ability to adapt to complex surfaces. These batteries have restricted form factors and inadequate mechanical flexibility for integration into devices [3–6]. In this context, the printing of batteries is a potentially innovative fabrication technique able to combine the benefits of thin-film technology, when considering the lightness, mechanical flexibility, easiness of integration, and additive manufacturing, in terms of low-cost production, scalability, versatility, and reproducibility [7,8].

Among the additive manufacturing technologies, inkjet printing represents a cost-effective, contactless droplet-based deposition technique [9,10]. However, the main bottleneck to obtaining a full inkjet-printed battery is printing the current collector (CC), whose role is to mechanically support and electrically bridge the electrodes to an external circuit [11]. CCs need to meet specific requirements in terms of a) *electrochemical stability* toward undesired redox reactions inside the potential window during charge/discharge processes, b) high *electrical conductivity*, as electrons generated need to be readily transferred to the external circuit, c) *low density,* because CCs are passive components and they do not participate in charge storage, d) *mechanical integrity*, as CCs also provide mechanical support to electrodes, in particular when they undergo volumetric expansion during cycling or deformation during use, and good electrode adhesion is required [12–14]. This last aspect is particularly significant when considering flexible cells.

Layered and planar (interdigitated) battery designs are both common, but very different [15]. The layered configuration involves the electrodes on different planes and the electrolyte sandwiched between the electrodes, optimizing the ionic diffusion path and electrode/electrolyte interfaces. However, this configuration doesn't favor mechanical flexibility. The planar configuration, instead, involves the two electrodes placed in the same plane and the electrolyte placed on top of the two surfaces. With this design, minimizing the distance between the electrodes becomes the main issue [16]. At the same time, this design represents an optimal configuration to best accommodate mechanical deformations, sensibly reducing the risks of short-circuits during deformations.

The most common CCs for lithium-ion batteries are aluminum, copper, stainless steel, and nickel [17]. Also, silver and gold are used, but not in large-volume industrial applications as they are expensive [18–20]. When dealing with inkjet printing of metallic nanoparticles, oxidation risk, and stability issues arise. Metal nanoparticles also require high sintering temperatures after printing, which are incompatible with the majority of flexible substrates. However, successful inkjet printing of metallic nanoparticles on flexible substrates has been demonstrated in a few cases [21–25]. In particular, Gu et al. obtained a nickel current collector through a reactive inkjet printing [26]. A cost-effective and easier option could be carbon-based CCs [27–32], but the lower conductivity compared to metal nanoparticles makes them inadequate for this application. Recently, an emerging class of 2D materials, MXenes, attracted attention because of their electrical, optical, and electrochemical properties. MXenes are transition metals carbides and/or nitrides, with general formula $M_{n+1}X_nT_x$, where M stands for a transition metal, X is either carbon and/or nitrogen (oxygen substitution is possible) and T_x represents surface terminations [33]. This work is focused on $Ti_3C_2T_x$ MXene, which is known for its high electrical conductivity (>20,000 S cm^{-1}), which makes it ideal for CC applications [34–36]. Moreover, the –OH and = O dominated surface terminations, T_x, make MXenes hydrophilic [37]. This is particularly convenient when dealing with inkjet printing, because of the easy and safe processing of aqueous inks [37,38]. In this context, Gogotsi et al. proved the feasibility of adopting $Ti_3C_2T_x$ MXene as a current collector [40].

This work aims to develop $Ti_3C_2T_x$-based inks for printed CC for an inkjet-printed lithium-ion battery with lithium titanate ($Li_4Ti_5O_{12}$, LTO) and lithium iron phosphate ($LiFePO_4$, LFP) electrodes. Different inks were tested from a rheological and dimensional point of view. $Ti_3C_2T_x$-based films were printed, and their electrical conductivity was studied, also under bending. Electrochemical characterizations involved testing $Ti_3C_2T_x$-based electrodes for electrochemical stability within the operating potentials window and electrochemical performance of the full batteries in the coin-cell and planar configurations.

2. Materials and experimental

2.1. $Ti_3C_2T_x$ MXene synthesis

$Ti_3C_2T_x$ MXene was synthesized through the mixed-acid method [34]. 1 g of Ti_3AlC_2 MAX phase was added to an etchant solution, composed of 2 mL of HF, 6 mL of distilled H_2O, and 12 mL of HCl. The solution was left under stirring at 300 rpm for 24 h and at 35 °C. The obtained multilayer $Ti_3C_2T_x$ was washed and centrifuged at 3500 rpm for 5 min until a pH of 5–6 was obtained. After washing, a delamination step was performed to obtain single-layer $Ti_3C_2T_x$. 1 g of LiCl and 100 mL of distilled H_2O were added to the neutralized multilayer $Ti_3C_2T_x$. The solution was left under stirring at 300 rpm for 24 h at 35 °C. The solution was then centrifuged at 3500 rpm for 5 min, discarding the clear supernatant and redispersing the deposit in distilled water. Centrifuge cycles at 3500 rpm for 45 min were repeated, each time collecting the dark supernatant that consisted of delaminated single-layer $Ti_3C_2T_x$ flakes.

2.2. Inks preparation

LTO and LFP-based electrodes were prepared according to Ref. [41], using multiwalled carbon nanotubes (MWCNT) as the conductive additive. These materials were used as purchased. $Ti_3C_2T_x$ ink was obtained by mixing 1.6 g of $Ti_3C_2T_x$ MXene and 50 mg of sodium ascorbate in 50 mL of deionized water. The mix was ultrasonically bathed for 30 min and then probe-sonicated for 15 min at 130 W (1.5 on, 1.5 off). Once everything was well dispersed, 0.03 g of lithium dodecyl sulfate (LDS) was added, and the solution was centrifuged for 10 min at 1500 rpm to remove any possible unetched residue or undesired phases.

2.3. Preparation of thin-film electrodes and devices

Coin cell configuration. All inks were transferred to properly cleaned HP45 cartridges and then inkjet printed using a flat-bed Breva thermal inkjet printer on a stainless-steel disc where a 1 mM polyethyleneimine (PEI) in ethanol was previously sprayed. The cartridge had an integrated printhead with 300 nozzles whose diameter was ~30 μm. Printer parameters were set to 11.5 V as pulse voltage and 2.2 μs as pulse duration. The printing process was repeated according to the needed electrode thickness.

Device configuration. Devices were obtained by printing an interdigitated pattern (area ~2 cm^2), first printing the current collector, i.e., $Ti_3C_2T_x$, on a polyethylene terephthalate (PET) substrate, where a thin film of PEI solution was sprayed. Then the LTO and LFP-based inks were printed separately, for the anodic and cathodic sites, respectively. Interelectrode distance was set to 500 μm and 800 μm. Printed electrodes/devices were then dried in an oven overnight before any characterization. In particular, the devices were placed in a 3D printed Polypropylene (PP) cell for the electrochemical characterization, necessary to contain the 2 M lithium bis(trifluoromethanesulfonyl)imide (LiTFSI) in propylene carbonate (PC) electrolyte. The 3D printed cell featured bumps with different bend radii, from 0° (flat condition) to 15°, 30° and 45°. 3D-printed caps were used to press the separator on the device.

2.4. Characterization

2.4.1. $Ti_3C_2T_x$ characterization

Imaging of $Ti_3C_2T_x$ MXene flakes was performed using a Zeiss Supra 50VP SEM. X-ray diffraction patterns were collected using a Rigaku SmartLab diffractometer with a Cu K_α source. MAX phase samples were scanned from 3 to 90° 2θ, while MXene samples were scanned from 3 to 70° 2θ. A current of 15 mA and a voltage of 40 kV were used with a step size of 0.02° 2θ and a duration time of 0.4 s. Optical properties analysis was conducted using an Evolution 201 UV–vis spectrophotometer (Thermo Scientific) with a 10 mm optical path length quartz cuvette. Spectra were collected from 200 to 1000 nm.

2.4.2. Inks characterization

Rheological properties were measured using an Antoon Paar rheometer (MCR-302) with a plane-plane geometry, with a gap of 0.2 mm and a material volume of 110 μl. A sample pre-shearing (at 1000 s^{-1} for 45 s) was performed to ensure that all samples had the same mechanical history. Viscosity was measured as a function of the shear rate from 0.1 to 10000 s^{-1}. Data are shown starting from 10 s^{-1}. Surface tension measurement was performed by pendant drop technique and drop shape analysis fitted through Opendrop software. Zeta potential and particle size distribution analyses were performed using a Zetasizer (Malvern Instruments).

2.4.3. Printed electrodes/devices characterization

Electrical resistance values of the $Ti_3C_2T_x$-printed patterns were measured using a two-point probe, through a multimeter (TRMS Fluke179), at a fixed distance. Images of printed $Ti_3C_2T_x$ ink on Kapton substrate and spacing between electrodes were obtained through optical microscopy using a Leica FTM200. The inkjet printed electrodes, i.e., LTO and LFP half-cells, were tested by assembling coin cells (CR2032) using Li foil as counter and reference electrode, Celgard 2400 as a separator, and 50 μl of 2 M LiTFSI in PC as electrolyte. Full LTO/LFP cells were assembled balancing the *N/P* capacity ratio to 1.1:1. The *N/P* ratio is defined by the following equation [42]:

$$\frac{N}{P} = \frac{q_{NE} m_{NE}}{q_{PE} m_{PE}} \quad (1)$$

where q_{NE} and q_{PE} are the gravimetric capacities of the negative and positive electrodes, and m_{NE} and m_{PE} are the negative and positive active material loadings, respectively. Coin cells were assembled in a glove box (MBraun) filled with argon gas (H_2O, O_2 < 0.5 ppm). Cyclic voltammetry (CV) curves were recorded using Biologic (VMP3 potentiostat) in a voltage window of 1–3 V vs Li^+/Li for LTO, 2.8–4 V vs Li^+/Li for LFP, 1–4 V vs Li^+/Li for $Ti_3C_2T_x$ and 1.25–2.5 V for LTO/LFP full cell using 1 mV s^{-1} as scan rate. Galvanostatic charge-discharge curves (GCD) curves were performed with a Neware cycle tester, in the same voltage windows previously mentioned at 0.5 C-rate. Electrochemical impedance spectroscopy (EIS) measurements were performed with Biologic in the frequency range 5 MHz–0.1 Hz and 10 mV pulse amplitude. The same sets of electrochemical experiments were performed on the device. All measurements were conducted at room temperature.

3. Results & discussion

3.1. $Ti_3C_2T_x$ MXene synthesis

Fig. S1a shows the XRD patterns of the precursor Ti_3AlC_2 MAX phase and the corresponding single layer (SL)- $Ti_3C_2T_x$ MXene phase, while the inset refers to a SL-$Ti_3C_2T_x$ free-standing film obtained through vacuum filtration. The XRD pattern of the MAX phase was characterized by the presence of all the typical crystallographic peaks, with no evidence of a TiC secondary phase [43,44]. The position of the 002 peak is indicative of successful etching and delamination, as a shift toward lower diffraction angles indicates an effective Al removal and introduction of surface terminations, which induces an expansion of the *d* spacing, i.e. substitution of Al with –F and –OH/ = O terminations [43]. The shift of the 002 peak toward lower diffraction angles, i.e. 7.72°, compared to the one of the MAX phase, i.e. 9.47°, confirmed a successful conversion to single layer $Ti_3C_2T_x$ MXene, resulting from Al etching and intercalation of Li^+ ions and water molecules [45]. This was confirmed by the fact that the corresponding interlayer distance was 2.97 Å for $Ti_3C_2T_x$ obtained through the mixed acids method, respectively. The size of Li^+ ions is approximately 0.9 Å, while the one of water is around 2.8 Å. This means that additionally to Li^+ ions, that were used to delaminate, also (partial) water molecules were intercalated. In addition, MAX phase XRD presented the characteristic set of high-order diffraction peaks located around ~ 39°, which was completely absent in the XRD pattern of $Ti_3C_2T_x$. The latter is characterized by the presence of only (00*l*) peaks when flakes are aligned in the plane [43]. A further investigation was performed using UV–vis spectroscopy to confirm the conversion of MAX to $Ti_3C_2T_x$. Fig. S1b reports a series of UV–vis spectra of $Ti_3C_2T_x$ dispersions with varying concentrations. Very diluted (≪ 0.5 mg L^{-1}) aqueous dispersions of $Ti_3C_2T_x$ produced a characteristic greenish color, that was used as a visual indicator of a good quality of the obtained $Ti_3C_2T_x$. UV–vis spectrum of the obtained $Ti_3C_2T_x$ diluted dispersion evidenced the presence of the characteristic plasmonic peak located at ~ 770–780 nm and the absence of the characteristic peak of Ti_2CT_x located around 550 nm [46]. Since the intensity of absorbance of the UV–vis peaks is proportional to the concentration of the solute, Lambert-Beer law was adopted (2), which allowed us to generate a calibration curve, where *A* is the absorbance, ε is the molar attenuation coefficient, *L* is the optical path length and *C* is the concentration of the attenuating species:

$$A = \varepsilon L C \quad (2)$$

Thus, by knowing the absorbance of the peak at 770 nm, it was possible to derive the concentration of diluted $Ti_3C_2T_x$ dispersions. Ultimately, another important characteristic to evaluate was the single flake dimensions, as size affects the electrical conductivity of the $Ti_3C_2T_x$ film. Larger flakes better overlap, creating a better percolative conductive network. MXene lateral flake size was measured by coupling DLS with SEM analysis. Fig. S1c reports the lateral flake size distribution obtained by DLS, coupled with an SEM image of a single flake $Ti_3C_2T_x$ MXene. Although direct microscopy measures are generally more complex and time-consuming, DLS offers a faster way to derive the size distribution. This involves, however, a methodological drawback when considering the light scattering particles as spherical, which is not the case for MXene flakes [43]. However, Maleski et al. [47] reported that DLS results were comparable with SEM. DLS analysis showed that the average size of as-synthetized flakes was around 1.3 μm, which was confirmed by the SEM images of single flakes. In addition, SEM enabled a qualitative analysis of the appearance of the flakes, which feature well-defined edges, with no evident defective sites, that are considered detrimental as they can favor pitting or oxidation onset. Ultimately, colloidal stability was measured by the zeta potential analysis which indicated a mean zeta potential of −44 mV, suggesting optimal dispersion stability. The morphology and elemental composition of Ti_3AlC_2 MAX phase and $Ti_3C_2T_x$ MXene were investigated through SEM analysis coupled with EDS. Fig. S2a shows the SEM image of the raw Ti_3AlC_2 MAX. A wide distribution of particle size was visible, ranging from tens of μm to a few μm. The corresponding EDS spectrum is reported in Fig. S2d, where the Al peak is well evident. After etching and delamination, $Ti_3C_2T_x$ MXene was obtained. Figs. S2b–c shows the SEM images of $Ti_3C_2T_x$ MXene powder and $Ti_3C_2T_x$ MXene flake stack, respectively. During drying of $Ti_3C_2T_x$, flakes spontaneously stacked one on top of each other, creating a lamellar structure, where the 2D sheets were clearly visible (Fig. S2c). As expected, the EDS spectrum of $Ti_3C_2T_x$ MXene was characterized by a drastic decrease of the Al peak, as a result of the etching. In addition, Cl and F terminations were introduced during

the etching and delamination steps, as shown by the rise of the Cl and F peaks in the EDS spectrum of $Ti_3C_2T_x$ MXene (Fig. S2e).

3.2. Inks rheology

Inkjet printing poses strict requirements in terms of ink viscosity, surface tension, and particle dimensions. To ensure a clogging-free jetting condition, ink viscosity should be lower than 15–20 cP according to the specific printer, surface tension should be comprised between 25 and 50 mN m^{-1}, while particles dimensions should not exceed 1/50 of the nozzle diameter (~31 μm).

Active materials (LTO/LFP). LTO ink formulation and characterization following ref. [41], using MWCNTs as the conductive agent. The same ink formulation and characterization procedure was adopted to produce the LFP-based ink. The rheological and physical properties are reported in Table 1. Flow curves of both active materials inks are reported in Fig. 1a. A Newtonian-like fluid behavior was obtained also for the LFP-based ink, as well as similar values of surface tension, density, mean zeta potential, and particle size values were obtained.

$Ti_3C_2T_x$ MXene. $Ti_3C_2T_x$ is characterized by outstanding hydrophilicity, thus stable water-based $Ti_3C_2T_x$ dispersions can be obtained with no particular effort, even by handshaking [48]. Despite different ink preparation protocols that have been proposed in literature [39,49–51], low-power probe sonication was adopted for producing a stable MXene ink. Fig. 1a compares the flow curves of the active materials inks and the one of $Ti_3C_2T_x$. In particular, viscosity values were taken in the high shear rate region, as here values are representative of the real viscosity of the ink during the ejection phase when high shear rates are involved.

While active material inks were more in line with a Newtonian-like behavior, $Ti_3C_2T_x$ ink was characterized by a shear-thinning behavior [52], which was as well desirable as no increase of viscosity was registered in the area of interest. In particular, it has been shown in the literature that it was possible to exfoliate multilayered $Ti_3C_2T_x$ particles and at the same time reduce the flake size through high-power probe sonication, which is particularly useful for printing applications where dispersions with sub-μm particles are employed to limit nozzle clogging during the ejection phase. However, the limitation of this approach is the excessive electrical degradation of MXene flakes, because of a substantial flake size reduction [47]. So, we decided to adopt a low-power liquid phase exfoliation to avoid this issue and select the optimal lateral flake size. Fig. 1b shows DLS curves associated with different probe sonication times. As-synthetized $Ti_3C_2T_x$ flakes were too large to be printed without probe sonication. In other words, the obtained size distribution was not compatible with inkjet printing, as 1.2 μm flakes would clog the nozzles. It was evident the disruptive effect as the sonication time increased: 3 min of impulse were sufficient to obtain an average flake dimension of about 600 nm, which was the largest flake size that could be printed in a clogging-free condition. The difficulty was to find a good trade-off between two opposite conditions: MXenes flakes should be as large as possible to ensure the highest electrical conductivity, but at the same time as small as possible to ensure a smooth printing step, without nozzle clogging. DLS analysis was then coupled with SEM technique to confirm the obtained results. The advantage of DLS is in general the possibility to measure particle size directly in the colloidal dispersion, avoiding the drying step, which, is necessary in direct microscopy techniques, such as SEM, that can alter the measurements because of agglomeration. However, the limitation of DLS is related to the assumption that particles in suspension are spherical, which is not the case for $Ti_3C_2T_x$ flakes. However, Lotya et al. [53] found a good empirical correlation between the hydrodynamic radius, a, and the average 2D lateral flake size, $< L >$ through the empirical equation:

$$< L >= (0.07 \pm 0.03)a^{(1.5 \pm 0.15)} \quad (3)$$

Fig. 1c shows the effect of probe sonication time on the final flake size, coupled with SEM images, which confirmed both the effect of probe sonication in decreasing the MXene flake size and the good correlation between DLS and SEM results. In addition, flakes showed well-defined edges, with no noticeable defects introduced by mild sonication. Fig. 1d shows the surface tension of the inks compared to pure water. The surface tension of all inks had to be adjusted through the addition of a surfactant, as the surface tension of pure water (~ 70 mN m^{-1}), is too high for inkjet printing. This was adjusted by adding 1.5 mM LDS, after which the surface tension value dropped to 35.7 mN m^{-1}, becoming compatible with the printing requirements. In addition to LDS, sodium ascorbate was added to the $Ti_3C_2T_x$ formulation to prolong the ink's lifetime. Prolonged storage of $Ti_3C_2T_x$ in water solutions is detrimental for $Ti_3C_2T_x$ properties as MXene oxidation by dissolved oxygen in water may lead to TiO_2 formation [54]. Reducing agents, i.e., sodium ascorbate and ascorbic acid, in low concentrations, improve the shelf-like of aqueous MXene dispersions, as they mask the flake edges, so where the most reactive sites are present. The drop formation behavior is generally described by the inverse of the Ohnesorge number $(Oh^{-1}) = (\gamma d\rho)^{1/2}/\eta$, where γ is the ink surface tension, d is the nozzle diameter, ρ is the ink density and η is the ink viscosity. For a stable drop formation, Oh^{-1} is expected to be between 1 and 10. However, if satellite drops can recombine with the main drop before hitting the substrate, higher values of Oh^{-1} are acceptable. $Ti_3C_2T_x$ ink Oh^{-1} value was 11.47, thus slightly outside the optimal range individuated by Derby and Reis. The *Oh-Re* printability diagram was constructed for the $Ti_3C_2T_x$ ink (Fig. 1e). However, similar results to the LTO *Oh-Re* diagram were obtained, since *Oh* values were slightly higher. Also, in this case, the optimal printing voltage was 11 V, as it was the one providing the optimal drop speed. Ultimately, mean zeta potential (ζ) was evaluated, as it represents an indicator of colloidal dispersion stability. If ζ is greater than ±30 mV, the colloidal dispersion is defined as stable. Based on this, good stability was found for LTO, LFP, and $Ti_3C_2T_x$ ink formulations (Table 1).

3.3. Substrate preparation & printed pattern characterization

Flexible batteries require a flexible substrate. Different approaches can be used in terms of substrate choice. However, a common denominator among all is substrate preparation, as it highly affects the final printing quality in terms of adhesion and resolution. For this specific application, we decided to adopt Mylar and Kapton substrates. Being hydrophobic materials, a surface pre-treatment was fundamental to obtain optimal ink wetting, which was crucial to favor a homogeneous material redistribution and drying. Substrate pre-treatment involved the application of corona treatment for 1 min, followed by spraying of 1% wt. polyethyleneimine (PEI) solution in ethanol. The thin PEI layer served as an adhesion layer for $Ti_3C_2T_x$, as PEI is positively charged and $Ti_3C_2T_x$ is negatively charged in aqueous solutions (zeta potential of

Table 1
Viscosity, surface tension, density, Oh^{-1}, and zeta potential values of $Ti_3C_2T_x$, LFP, and LTO inks.

	Viscosity (cP)	Surface tension (mN m^{-1})	Density (kg m^{-3})	Oh^{-1}	ζ (mV)
$Ti_3C_2T_x$	2.58	49.3	1030	13.47	−37.3
LFP	2.71	40.94	1040	12.92	−36.4
LTO	2.82	40.41	1040	12.34	−39.6

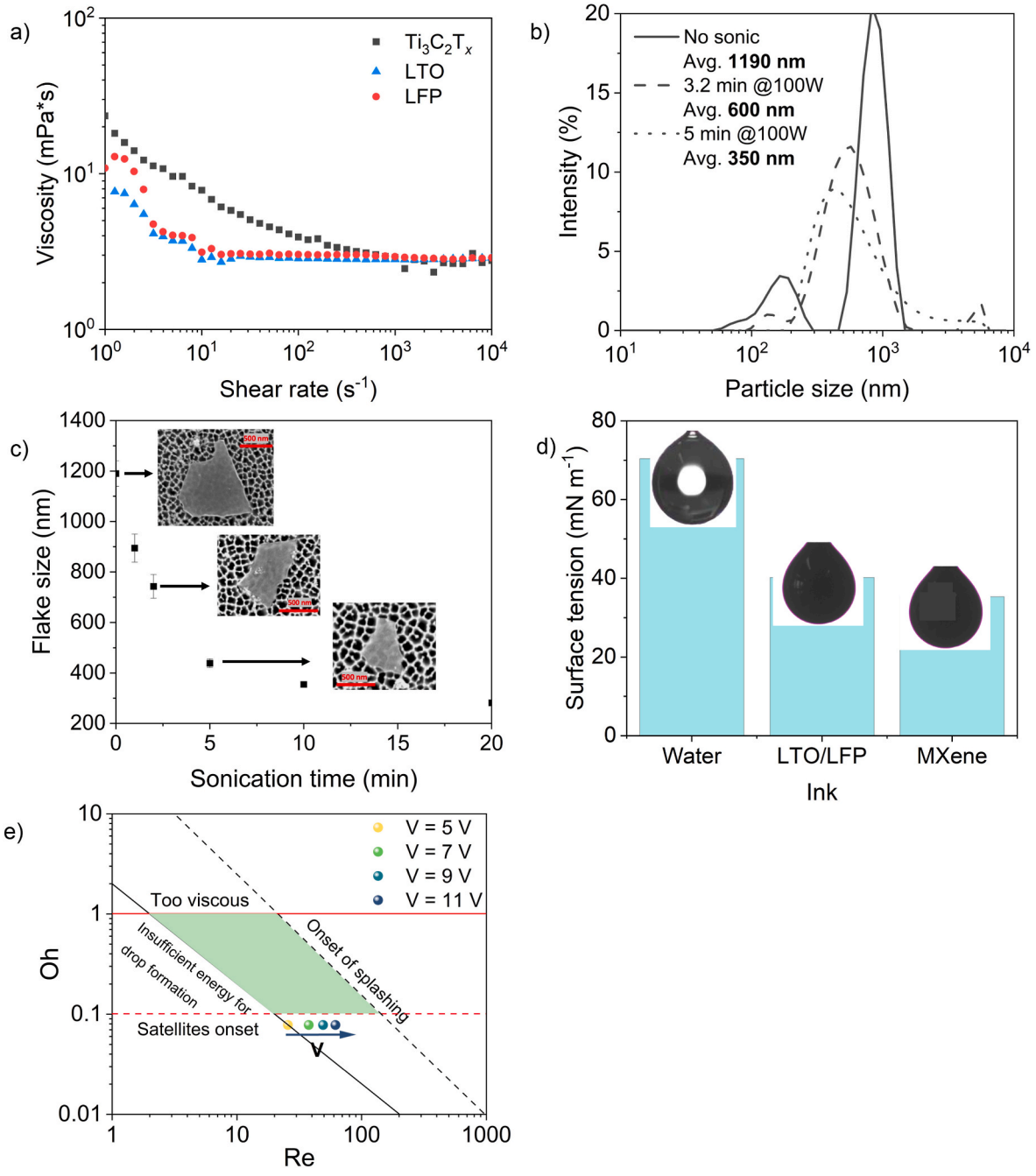

Fig. 1. Flow curves of LTO (blue triangles), LFP (red circles) and $Ti_3C_2T_x$ (black squares) inks (a), Particle size distribution profiles of $Ti_3C_2T_x$ inks, not sonicated (solid), 3 min (dashed) and 5 min sonication (dotted) (b), flake size as a function of sonication times coupled with SEM images of $Ti_3C_2T_x$ single flakes (c), surface tension values of pure water, LTO/LFP and MX inks and relative pendant drop images (d) and *Oh-Re* printability diagram of $Ti_3C_2T_x$ ink upon voltage variation (e). (For interpretation of the references to color in this figure legend, the reader is referred to the Web version of this article.)

−37 mV), thus an electrostatic interaction was built. In addition, PEI was used to favor a good wettability of the aqueous-based ink on plastic-based substrate. Fig. S3 a-b shows the difference between a non-treated and a PEI-treated surface, respectively, after printing $Ti_3C_2T_x$ ink. PEI activation was crucial to obtain optimal ink wetting and continuous and homogeneous printed layers, which affected the final conductivity, which will be considered in the next paragraph. Static water contact angle (WCA) was used to evaluate the best surface activation and ink-wetting conditions. Fig. S3 c-e refers to WCA on non-treated Mylar and Kapton substrates of 73° and 88°, respectively, indicating a hydrophobic behavior of the substrate, which didn't allow a good wetting of the particle. These values decreased to ∼ 22–24° after treating the substrate with PEI, demonstrating an improved wettability of the substrate. Fig. S3 d-f reports the decreased WCA on PEI-treated PET and Kapton substrates, respectively. However, it is important to underline that a WCA ≪ 10° was undesired, as this corresponded to a complete broadening of the drop due to excessive hydrophilicity of the substrate, risking the low quality of the final printing resolution as drop shape retention cannot be achieved. A patterned planar design was adopted to produce the battery device. Good electrode adhesion to the substrate was crucial to have a good performing cell with flexibility properties [12–14]. The device model is reported in Fig. 2a. The device was characterized by a varying number of printed layers of $Ti_3C_2T_x$ CC, which was the layer printed directly in contact with the substrate, and of

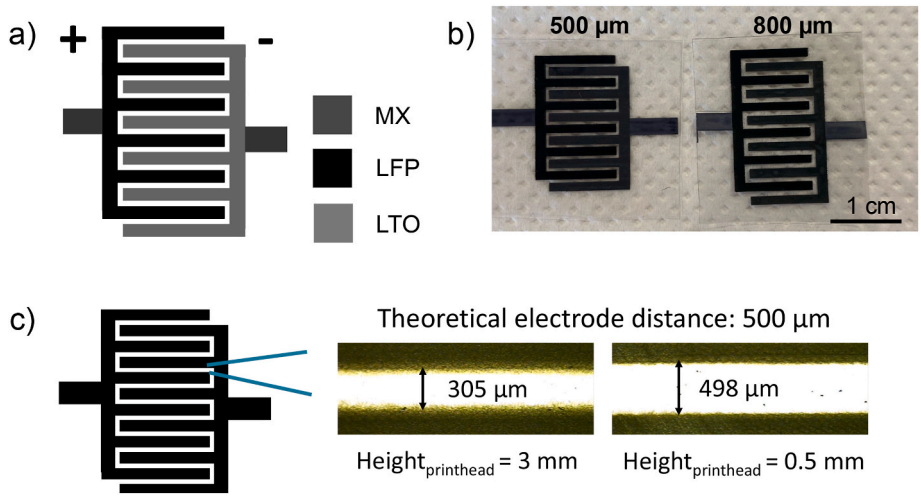

Fig. 2. Device planar electrode model, showing the MXene current collector, LTO printed on the negative site and LFP printed on the positive site (a), printed planar device on PET substrate, with different interelectrode distance: 500 µm (left) and 800 µm (right) (b) and printhead height effect on the obtainment of the theoretical interelectrode distance (c).

LTO and LFP electrodes, printed on the respective negative and positive sites. The electrolyte was placed on top. Two examples of cells were reported with distances (gaps) between interdigitated electrodes of 500 µm and 800 µm (Fig. 2b). In this case, the interelectrode distance was a key parameter, as a lower distance favors lower internal resistances because of a shorter Li^+ ions diffusion path. However, the possibility to reduce such distance was determined by the printer resolution. We found that the shortest interelectrode distance that was possible to print without causing a short circuit was 500 µm, which was very high, especially if compared to the separator thickness (less than 25 µm) typically employed in coin cells. Ultimately, we observed that pattern resolution depended on the printhead height: a target electrode distance was set to 500 µm. Fig. 2c highlights the importance of the printhead height with respect to the substrate during printing on the final printing resolution. Printhead height needed to be accurately chosen, as a higher distance caused the deviation of the drop from the ideal perpendicular path from the printhead to the substrate, thus lowering the resolution. Indeed, using a higher printhead height (3 mm), a smaller distance between the electrodes and less defined edges were obtained. Non-controlled electrode distance was not desired as short circuits were likely to happen due to electrode bridging because of mispositioned drops.

3.4. Electrical characterization of $Ti_3C_2T_x$ printed patterns

Three free-standing films of as-synthetized $Ti_3C_2T_x$ were vacuum-filtered with different thickness, which was measured through a micrometer and SEM cross-sections. Fig. S4a reports three free-standing films coupled with their respecting SEM cross-sections. Conductivity values of different free-standing films were obtained after measuring the sheet resistance (R_s) with a four-point probe in five different points that are reported in Fig. S4a. Conductivity σ was calculated through the equation:

$$\sigma = \frac{1}{\rho} = \frac{1}{R_s t} \tag{4}$$

where ρ is the resistivity and t is the film thickness. The obtained conductivities were in the range of 8–9 kS cm^{-1}, as seen in Fig. S4b, which was associated with flakes in the order of 1–1.2 µm. However, IJP of flakes in the order of µm would likely cause nozzle clogging. Thus, two other free-standing films were vacuum filtered from $Ti_3C_2T_x$ suspensions characterized by different flakes size, i.e., 600 and 350 nm, and again the respective conductivities were measured and compared with the one obtained from as-synthetized $Ti_3C_2T_x$ flakes suspensions. Table 2 compares how the conductivity changed upon lateral flakes dimension. As expected, the resistivity dropped from ~8 kS cm^{-1} to ~3700 S cm^{-1} when lowering flake dimensions to 350 nm. For this reason, $Ti_3C_2T_x$ suspension with lateral flake size of 600 nm was chosen as the one for IJP of the current collector, as it represented a good trade-off between the two opposite previously mentioned conditions.

The inset in Fig. 3a shows $Ti_3C_2T_x$ stripes of 6 cm where the width and number of printed layers were varied. The effect of width as well as the number of printed layers variation on the linear resistance of $Ti_3C_2T_x$ stripes was investigated using a two-probe multimeter. Fig. 3a shows the obtained results relative to the liner resistance (R_L) variation by varying the number of printed layers and stripes width. As expected, resistance values decreased by increasing the number of printed layers, as a better percolative conducting path was obtained among $Ti_3C_2T_x$ flakes. In addition, resistance values decreased by increasing the stripe lateral width, by the inverse proportionality of resistance with stripe width given by equation:

$$R_L = \frac{\rho}{W L} \tag{5}$$

where ρ is the material resistivity, L is the stripe length and W is the stripe width. In particular, for 20 printed layers, R_L values were 110.9 Ω cm^{-1} for a 1 mm wide stripe, 42.3 Ω cm^{-1} for a 3 mm wide stripe, and

Table 2
Sheet resistance, thickness, and conductivity of $Ti_3C_2T_x$ free-standing films characterized by different flake dimensions.

	Sheet resistance (Ω cm)	Thickness (µm)	Conductivity (S cm^{-1})
$Ti_3C_2T_x$ – 350 nm	0.562 ± 0.0032	4.7 ± 0.3	3786.47
$Ti_3C_2T_x$ – 600 nm	0.353 ± 0.0045	4.9 ± 0.3	5882.21
$Ti_3C_2T_x$ – 1.2 µm	0.185 ± 0.007	5.4 ± 0.2	8752.65

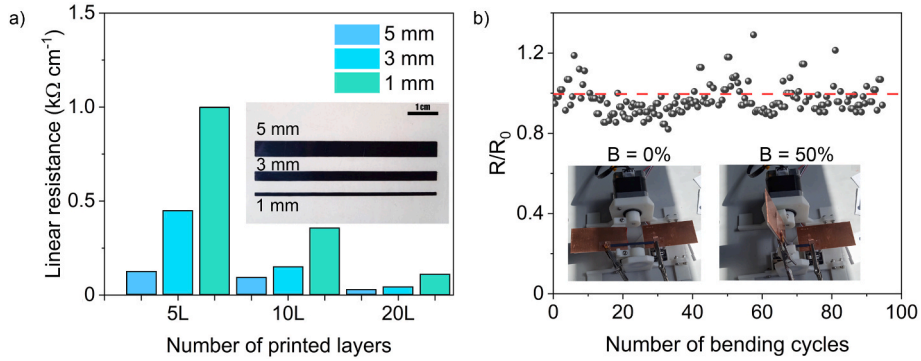

Fig. 3. Linear resistance variation as a function of the number of printed layers and stripe width, inset shows an optical image of $Ti_3C_2T_x$ printed stripes (20L) on PET varying width, i.e., 5 mm, 3 mm and 1 mm (a) and electrical resistance retention of $Ti_3C_2T_x$ printed stripe (20L) upon cycling between flat ($B = 0\%$) and bent ($B = 50\%$) conditions (b).

25.4 Ω cm^{-1} for a 5 mm wide stripe. In addition, the flexibility of the as-printed MXene layers was evaluated, by considering the effect of the bending ratio (B%), which is defined as:

$$B\ (\%) = \frac{L_0 - L}{L_0} \tag{6}$$

where L_0 is the stripe length under flat conditions and L is the distance between the stripe's edges once bent at a certain degree angle. Electrical resistance was monitored in flat ($B = 0\%$) conditions and at a bending ratio of 50%, corresponding to a stripe bending of 90°, using a custom-built apparatus equipped with a step motor rotating at 15 rpm. Fig. 3b shows the variation of the linear resistance normalized over the one in flat conditions (R/R_0) upon cycling of a 5 mm wide $Ti_3C_2T_x$ printed stripe (20L), where one cycle corresponded to stripe bending from 0% (inset on the left) to 50% (inset on the right) back to the flat condition. The obtained mean value of R/R_0 over 100 cycles was 0.97 ± 0.06, very close to 1, which corresponded to the optimal condition where no resistance variation compared to the one in flat conditions was observed. Interestingly, no evident resistance increase was observed at $B = 50\%$, demonstrating negligible electrical degradation and good conductivity retention upon bending conditions. This aspect posed good premises, as $Ti_3C_2T_x$-based CC demonstrated good flexibility properties. Fig. 4 shows SEM images of 20L $Ti_3C_2T_x$ printed lines in flat (4a, 4c) and after bending (4b, 4d). SEM images revealed well-defined edges, with no evident print mistakes, such as satellite drops, and the absence of severe cracks evidence even after bending. EDS spectra (Fig. 4e and f) showed a uniform distribution of Ti along the print with no evident agglomerations and depleted areas, demonstrating a final good print quality.

3.5. Electrochemical characterization of $Ti_3C_2T_x$ printed current collectors

CC must meet the precise requirements that were mentioned in the introduction. The electrical properties of $Ti_3C_2T_x$ printed patterns were investigated in the previous paragraph. Electrochemical characterization was performed at coin and device levels, to understand whether an inkjet-printed $Ti_3C_2T_x$-based current collector could represent a valid alternative to more traditional CCs, especially when considering patterned battery devices. The electrochemical performance of as-printed $Ti_3C_2T_x$ electrodes was tested, to assess whether a competitive redox reaction is occurring inside the operating potential window. A varying number of $Ti_3C_2T_x$ layers, i.e. 10, 20, and 35 layers, were printed on stainless steel separators and tested versus lithium as counter and reference electrode in coin configuration. Fig. 5a shows cyclic voltammograms of $Ti_3C_2T_x$-based electrodes with 10, 20, and 35 printed layers. CVs were performed and compared at 1 mV s^{-1}, using 2 M LiTFSI in PC as an electrolyte in the electrochemical voltage window of interest. Results have shown that the current response was rather low and slightly increasing with $Ti_3C_2T_x$ content in the electrode, demonstrating a desired redox inactivity of $Ti_3C_2T_x$ in the voltage window of interest, which was regarded as a key CC property. 20 layers of LTO were then printed on three $Ti_3C_2T_x$-based current collectors with different thicknesses and on a more traditional copper current collector. Fig. 5b shows the respective GCD curves obtained at 0.5 C-rate. LTO electrochemical performances were not altered when adopting a $Ti_3C_2T_x$-based current collector compared to a copper current collector, i.e., gravimetric capacity values were 171.3 mAh g^{-1} and 173.8 mAh g^{-1}, respectively, with a slight decrease in the gravimetric capacity when decreasing the number of printed $Ti_3C_2T_x$ layers. These results suggested a beneficial effect of using a $Ti_3C_2T_x$-based CC. We have derived the gravimetric energy density (GED) for the four coins according to equation (7), considering that only the mass of the current collector was varying:

$$GED\ (\mathrm{Wh\ kg^{-1}}) = \frac{V\,C}{m} \tag{7}$$

where V is the cell voltage, C is the cell capacity and m is the "battery" mass. However, there is no agreement on how GED values should be reported in the energy storage community, as different levels of focus, i.e. material, electrode, and device level, can be considered [55]. Thus, according to the considered level, different components' mass can be considered in the GED calculation, so that comparison among different materials becomes challenging. Firstly, in the calculation of this work, the mass of the package was not considered since it strictly depends on the final application and a plausible approximation of the mass is hard to do. Thus, the denominator m in equation (7) was calculated considering the mass of both the electrodes, the current collector, the electrolyte, and the separator. Practically, only the current collector weight was varying among the four considered coins.

By decreasing the overall battery weight, it was possible to improve the coin GED. Generally, decreasing the weight of battery inactive parts is beneficial, i.e., current collector or separator, as they are not contributing to the battery capacity. On the contrary, decreasing the weight of active components, i.e., electrode's active materials, and electrolyte, may have a detrimental effect on the GED as the capacity may be affected. Fig. 5c compares the calculated GED for four coins where only the CC was varied. Results have shown that the GED associated with the coin where the thinnest $Ti_3C_2T_x$ was adopted was increased by 21% compared to one where copper was used as CC. This was mainly attributed to sensibly lower $Ti_3C_2T_x$ density compared to copper one, i.e., 3 g cm^{-3} vs 9 g cm^{-3}, respectively, combined to lower $Ti_3C_2T_x$ thicknesses achieved with IJP. This aspect satisfied a further requirement of current collectors in terms of low density. Fig. 5d may help visualize the respective percentage that each battery component has on the overall battery weight. Again, Cu CC covered about 11% of the overall considered components mass, while the 1.7 μm $Ti_3C_2T_x$ CC covered about 1%.

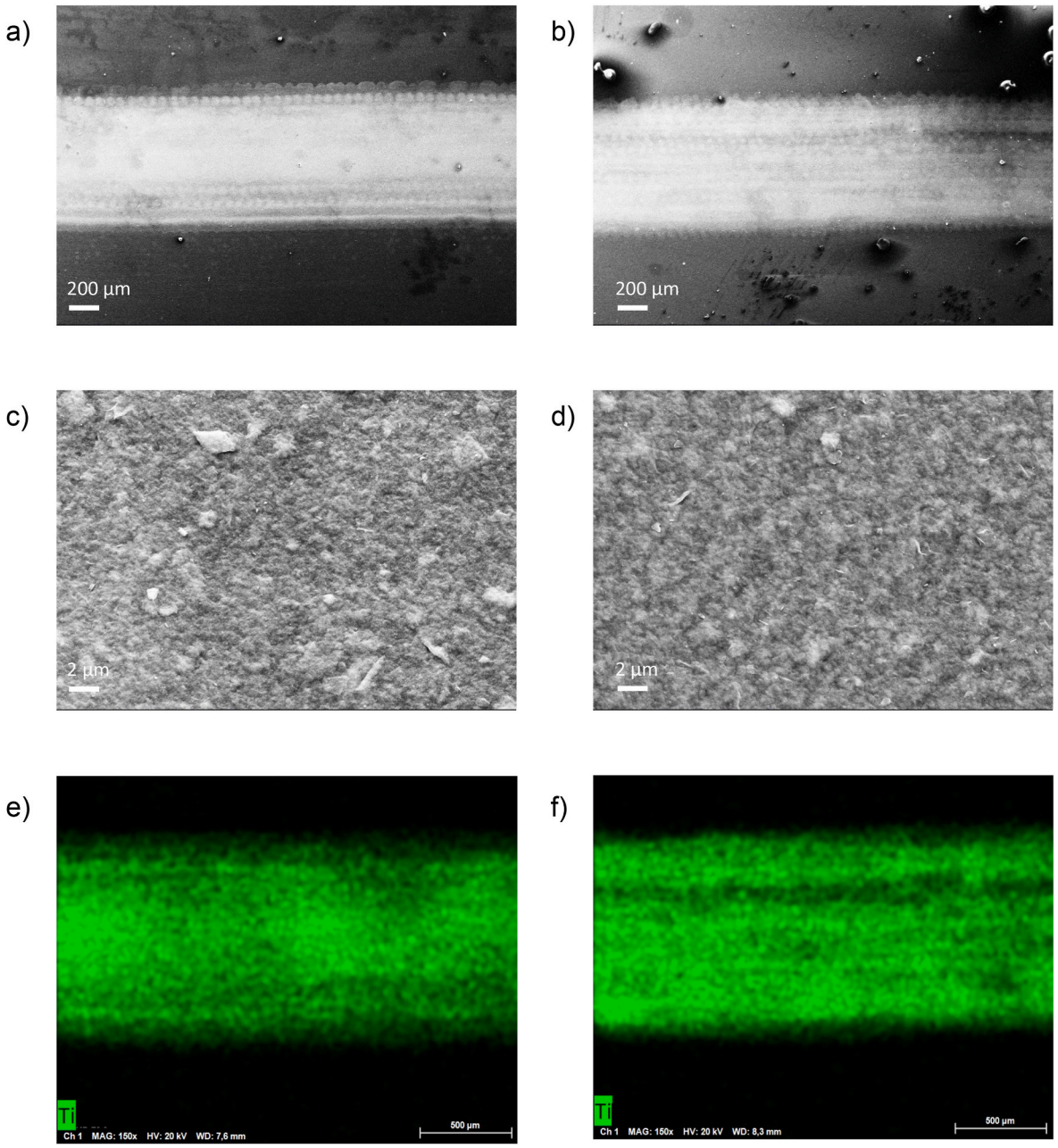

Fig. 4. SEM images of flat 20L printed $Ti_3C_2T_x$ at 100 X (a) and 10K X (c) and of bent 20L printed $Ti_3C_2T_x$ at 100 X (b) and 10K X (d). EDS spectra of Ti signal flat 20L printed $Ti_3C_2T_x$ (e) and of bent 20L printed $Ti_3C_2T_x$ (f).

3.6. Half and full cell electrochemical characterization – coin level

The $Ti_3C_2T_x$-20L electrode was adopted as a current collector for an LTO/LFP full cell, where LTO was chosen as the anodic electrode and LFP as the cathodic one. In particular, LTO is a promising anodic material, as it undergoes almost null deformation during the intercalation/deintercalation processes, which improves the material shelf life, and its electroactivity is at voltages > 1V vs Li^+/Li, preventing anode passivation and electrolyte decompositions. LFP, instead, is known because of its thermal and structural stability and high-rate performances. Electrochemical characterization of the LFP half-cell was performed and coupled with the one of LTO, presented in the previous chapter. Fig. S5a compared the CV of 20 layers $Ti_3C_2T_x$ electrode, CVs of printed LTO and LFP on 20 layers $Ti_3C_2T_x$ electrodes ions in the host material, i.e. 1.43 V and 1.71 V of LTO half-cell, and 3.1 V and 3.77 V of LFP half-cell, respectively. Likewise, the full LTO/LFP cell showed reversible redox peaks at 1.7 V and 2.02 V, which are typically associated with reaction (8).

$$Li_4Ti_5O_{12} + Li_{1-x}FePO_4 \leftrightarrow Li_{4-x}Ti_5O_{12} + LiFePO_4 \quad (8)$$

Lastly, the $Ti_3C_2T_x$-20L electrode showed a relatively low current response in the electrochemical window, indicating the electrochemical stability of $Ti_3C_2T_x$ as CC in the voltage window of interest. However, a slight increase in current response was observed at lower voltages, more specifically in the potential window of LTO. This aspect didn't affect the LTO capacity, as in this case, no evident contact between electrolyte and $Ti_3C_2T_x$ was present. In this context, the MXene layers work only as electrochemically inert current collectors. To understand the electrochemical performance in terms of storage capacity, galvanic charge-discharge (GCD) curves were obtained at 0.5 C. Fig. S5b displays the potential profiles as a function of the gravimetric capacity of the LTO/Li and LFP/Li half cells and the LTO/LFP full cell. LTO/Li and LFP/Li half

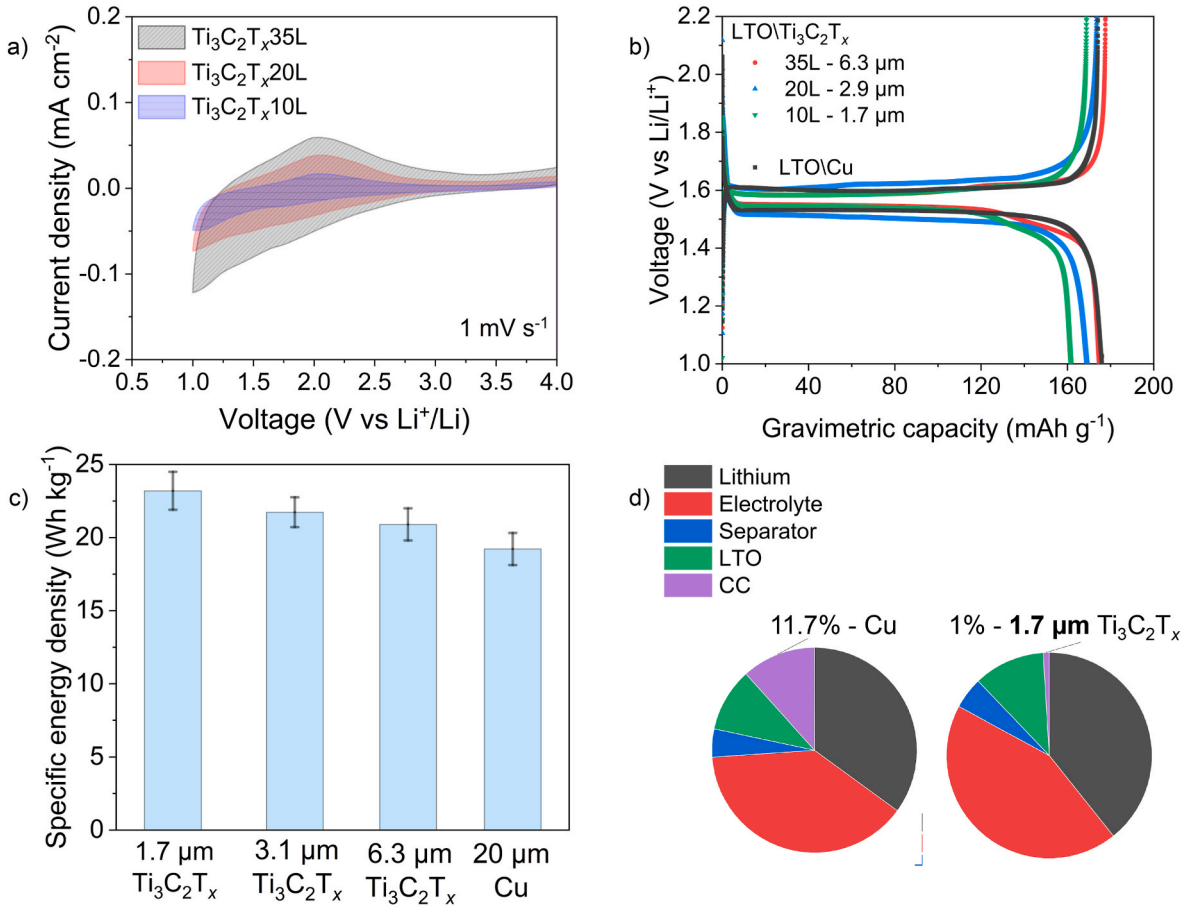

Fig. 5. Cyclic voltammetry of printed $Ti_3C_2T_x$ electrodes with different numbers of printed layers (a), GCD curves obtained at 0.5 C of LTO electrodes printed on 35 layers on $Ti_3C_2T_x$ (red), 20 layers (blue), 10 layers (green) and on copper current collector (black) (b), gravimetric energy density change upon current collector mass variation (c) and pie charts representing the percentage that each battery component has on the overall battery weight (d). (For interpretation of the references to color in this figure legend, the reader is referred to the Web version of this article.)

cells showed characteristic plateaus around 1.5 V and 3.5 V vs Li^+/Li, respectively. In particular, the LTO electrode was characterized by a specific capacity of 158 mAh g^{-1} with a Coulombic efficiency of 99%, while the LFP half-cell was characterized by a specific capacity of about 150 mAh g^{-1} with a Coulombic efficiency of 96%. As expected, the full-cell LTO/LFP voltage characteristics were found in between those of LTO/Li and LFP/Li, with characteristic plateau found around 1.8–1.9 V corresponding to a specific capacity of 113.1 mAh g^{-1} for the charge process and 110.3 mAh g^{-1} for the discharge process at 0.5 C. GCD tests were performed on the LTO/LFP full cell at different C-rate. Results are shown in Fig. S5c. In particular, the full cell showed a gravimetric capacity of 115 mAh g^{-1} at 0.2 C, 95 mAh g^{-1} at 0.5 C, and 87 mAh g^{-1} at 1 C. After cycling at 1 C, the capacity value matched the initial one at 0.2 C, indicating good cyclability of the cell, while the average Coulombic efficiency was around 96%.

3.7. Full cell electrochemical characterization – device level

Full cell LTO/LFP characterization was then performed at the device level. The device was mounted on a 3D-printed polypropylene cell. Four cells were printed, featuring different bending radii, i.e., 0°, 15°, 30°, and 45°, to test different degrees of device flexibility. Fig. S6 shows the CAD designs of the bottom side of the 3D printed cell featuring bumps with different bending radii, i.e., 15° (Fig. S6a), 30° (Fig. S6b), and 45° (Fig. S6c). Fig. S7 shows the device assembly process in the 3D printed cell with a bending ratio of 0° (flat condition). The device was placed on the bottom side of the cell on top of a gasket and copper contacts were connected (a), a separator was placed on top of the device (b), and a second gasket was placed (c) before closing the cell with the upper side (d). Ultimately, the cell was sealed with screws and an electrolyte was added to the device (e). Copper contacts were electrically connected to the $Ti_3C_2T_x$ current collector, and the electrolyte was contained in the gap facing the device. The electrolyte used was a 2 M lithium bis(trifluoromethanesulfonyl)imide solution in propylene carbonate and 1.5 ml of the solution was sufficient to fully cover the whole device surface. Moreover, capacity balancing was a crucial aspect to consider, to extract the full capacity of the full cell and to improve safety and lifetime, and it is usually evaluated considering the *N/P* ratio, defined by equation (1). For LIBs, *N/P* is currently controlled between 1.03 and 1.2, thus with an excess of lithium available in the anode with respect to that of the cathode. A low *N/P* ratio can favor the reduction of the anode potential <0 V vs Li^+/Li, thus favoring lithium plating on the anode electrode surface. Lithium plating, instead of intercalation, can occur under severe conditions of charging, such as charging at high current density, due to the sluggish Li^+ ions kinetic of the intercalation process, and must be avoided as causes degradation of the cell. Specifically, the plating of lithium generally leads to the growth of Li dendrites that can cause short-circuits, which can result in reliability and safety issues of the

Table 3
Number of LTO and LFP printed layers corresponding to a specific *N/P* ratio.

	N/P = 1.5	*N/P* = 1.2	*N/P* = 1.1	*N/P* = 1	*N/P* = 0.8
LFP	25	25	30	30	35
LTO	40	35	35	30	25

battery [56]. On the contrary, a too high *N/P* ratio may cause overcharging of the cathode, which damages both the material crystallographic structure and causes oxidation of the organic electrolyte [57]. So, we investigated the effect of different *N/P* ratios, controlling the number of printed layers. Table 3 reports the number of LTO and LFP printed layers corresponding to a specific *N/P* ratio. Fig. 6a reports the GCD test results in terms of gravimetric capacity upon current density variation. Non-optimized *N/P* ratios, i.e., $N/P = 1.6$, $N/P = 1$, and $N/P = 0.8$, were the ones providing the lowest gravimetric capacity, i.e. 3.12 mAh g^{-1}, 1.67 mAh g^{-1} and 1.09 mAh g^{-1} at a current density of 12.5 μA cm^{-2}, respectively, as capacity balancing between the negative and positive electrodes was not optimal and the capacity could not be fully extracted. $N/P = 1.2$ was the one providing the highest gravimetric capacity, i.e., 6.09 mAh g^{-1} at a current density of 12.5 μA cm^{-2}, which corresponded to 35 printed layers of LTO and 25 printed layers of LFP. Consequently, the following electrochemical characterization was done considering this combination of LTO and LFP printed layers, that were alternatively printed on 20 layers of $Ti_3C_2T_x$.

The electrochemical behavior of the battery device featuring different degrees of bending was first evaluated through cyclic voltammetry (CV), as reported in Fig. 6b. All CVs were recorded at 1 mV s^{-1} scan rate, using 2 M LiTFSI in PC from 1.2 to 2.2 V vs Li^+/Li. CVs revealed the presence of two reversible redox peaks associated with the highly reversible reaction of Li^+ ions intercalation/deintercalation inside the spinel and olivine structures of LTO and LFP, respectively. The cathodic reduction peak was located at 1.74 V, while the anodic oxidation peak was located at 1.98 V and was associated with the redox reaction [7]. The electrochemical performance was not affected by the bending of the device, i.e., peak intensity and position in terms of voltage were not varied upon the bending degree. The difference between the potentials of the anodic and cathodic current peaks is defined by:

$$\Delta E^{p} = E^{an,p} - E^{cat,p} \quad (9)$$

and can be interpreted as an indicator of possible polarization, that affects the overall performance of the device. Since ΔE^p variation between the different degrees of bending was negligible, no detrimental effects on the electrochemical behavior of the battery were evidenced upon bending. Fig. 6c shows the results of GCD tests of the devices with different degrees of bending, in terms of gravimetric capacity. Coherently with the results obtained with CV, the gravimetric capacity was not affected by different degrees of bending, demonstrating the flexibility of the device. Moreover, despite the low gravimetric capacity, i.e. ~ 6 mAh g^{-1}, the devices demonstrated a good rate capability even for a large number of cycles. Ultimately, Fig. 6d shows the resulting Nyquist plots of the devices with different bending degrees at the pristine state and after being cycled for 100 cycles and the equivalent circuit used for the fitting. In both, the pristine and cycled states, the charge transfer resistance R_2 was not affected by the increase of the bending angle, confirming the good flexibility of the device. After 100 cycles, the charge transfer resistance R_2 increased from a mean value of 144.79 Ω at the pristine state to a mean value of 225.2 Ω, probably due to partial delamination of the layers. Values of R_1 and R_2 obtained from the fitting are reported in Table 4. From the morphological point of view, no evident signs of cracking or damage were evidenced.

Ultimately, two devices were connected in series, to provide sufficient voltage, i.e., power, to power a blue LED ($V_{on} > 2.6$ V). First, a CV was performed to stabilize the system. Fig. 7a shows the sequence of techniques to which the series system under 45° bending conditions was subjected. The system was charged up to 3.9 V at 60 μA charging current (charging phase, light green line), after which 10–15 min waited to let the OCV adjust (OCV, dark green line). Once OCV was adjusted to a constant value, the switch button was pushed and the blue LED was powered on (discharging phase, blue line). Fig. 7b shows the series device under 45° bending conditions when the circuit was closed, i.e., blue LED was on. Ultimately, an amperemeter was connected to measure the current while discharging to calculate the areal power dispensed from the device, i.e., ~ 0.35 mW cm^{-2}, considering an area of 4 cm^2, which is

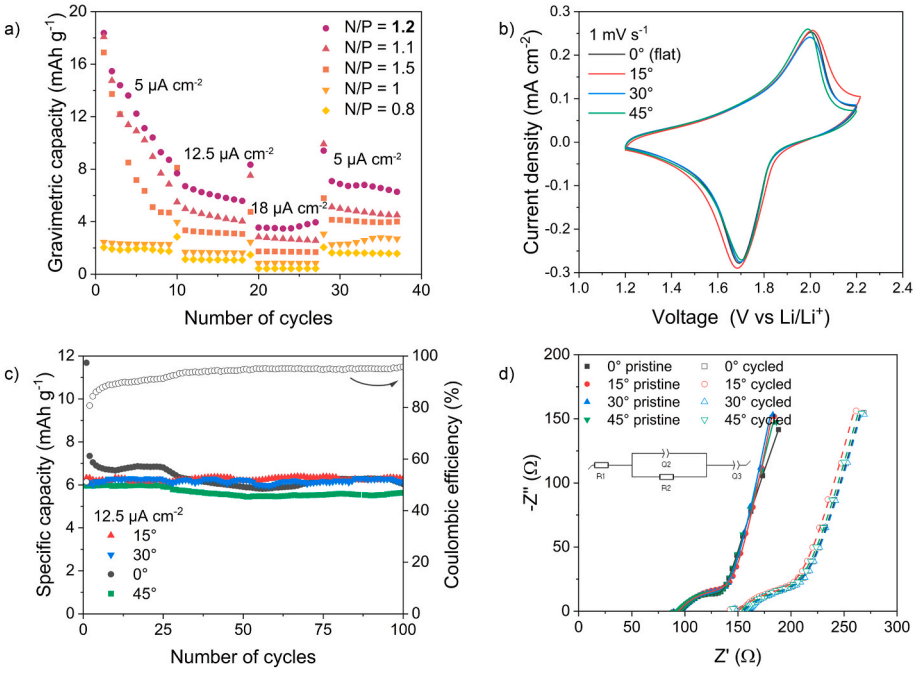

Fig. 6. Study of the optimal *N/P* ratio in terms of gravimetric capacity variation upon applied current density and *N/P* ratio (a), CVs of devices consisting of 35L of LTO, 25L of LFP on 20L of $Ti_3C_2T_x$ with different bending degree, i.e. 0° (black), 15° (red), 30° (blue) and 45° (green), at 1 mV s^{-1} (b), the gravimetric capacity of devices consisting of 35L of LTO, 25L of LFP on 20L of $Ti_3C_2T_x$ with different bending degree, i.e. 0° (black), 15° (red), 30° (blue) and 45° (green), applying a current density of 12.5 μA cm^{-2} (c) and Nyquist plots of the same devices with different bending degree, i.e. 0° (black), 15° (red), 30° (blue) and 45° (green), at the pristine (full) and cycled state (blank), inset: equivalent circuit used for fitting (d). (For interpretation of the references to color in this figure legend, the reader is referred to the Web version of this article.)

Table 4
R_1 and R_2 values obtained from fitting devices with different bending degrees in the pristine (P) and cycled (C) states, i.e., after being cycled for 100 cycles.

	0° (P)	0° (C)	15° (P)	15° (C)	30° (P)	30° (C)	45° (P)	45° (C)
R_1	94.35	154.9	92.27	150.2	94.4	155.3	93.85	153.1
R_2	137.31	226.64	146.21	221.12	152.19	228.61	143.45	224.46

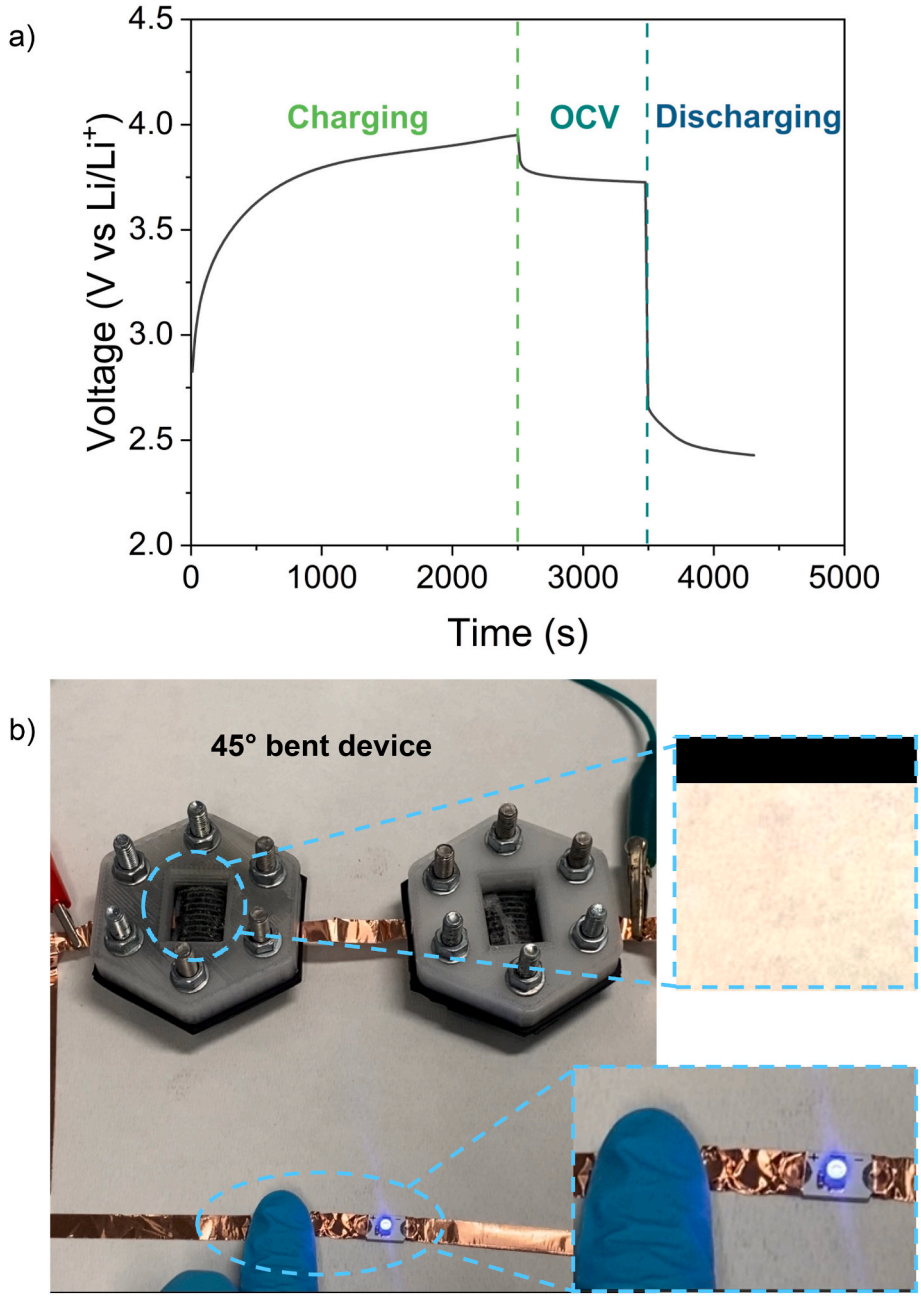

Fig. 7. The sequence of techniques at which the series system under 45° bending was subjected: charging (light green), OCV (dark green), and discharging (blue) (a) and image of the series system under 45° bending conditions at the closed circuit (LED is ON) (b). (For interpretation of the references to color in this figure legend, the reader is referred to the Web version of this article.)

only an order of magnitude lower compared to a typical value of the areal power density of common electronic devices, i.e., 10^1–10^3 mW cm^{-2}. Further improvement in the electrochemical performance, in particular the areal capacity of the device, is still necessary for practical use. This may be achieved by minimizing the spacing between the electrodes using a printer with a higher resolution.

4. Conclusions

This work has demonstrated the possibility of adopting $Ti_3C_2T_x$ as an alternative current collector material to replace metals. In particular, $Ti_3C_2T_x$'s hydrophilicity made it an optimal material for water-based ink for ink-jet printing, which does not require surfactants or stabilizing additives. The printed $Ti_3C_2T_x$ current collectors were characterized in

terms of their conductivity by varying the number of printed layers. Their flexibility was tested under multiple bending cycles and no significant change in the linear resistance was observed upon bending between 0° and 90°. The printed $Ti_3C_2T_x$ current collectors were then electrochemically characterized and showed no redox activity within the voltage window of interest, thus acting as passive elements. We have demonstrated that the electrochemical performance of LTO was the same with the printed $Ti_3C_2T_x$ and a traditional Cu current collector. An increase of 21% in gravimetric energy density was achieved when using $Ti_3C_2T_x$ instead of the Cu current collector, because of the lower density and thickness of the former. We also demonstrated printing the entire flexible battery. The electrochemical testing of a printed LTO/LFP cell with $Ti_3C_2T_x$ current collectors showed that bending didn't affect the performance of the cell. This result was confirmed by using multiple electrochemical techniques.

CRediT authorship contribution statement

Prisca Viviani: Writing – review & editing, Writing – original draft, Methodology, Investigation, Formal analysis, Data curation, Conceptualization. **Eugenio Gibertini:** Writing – review & editing, Methodology, Investigation, Formal analysis, Conceptualization. **Paolo Fontana:** Writing – review & editing, Investigation, Formal analysis, Conceptualization. **Federico Lissandrello:** Writing – review & editing, Investigation, Formal analysis. **Yury Gogotsi:** Writing – review & editing, Supervision, Project administration, Conceptualization. **Luca Magagnin:** Writing – review & editing, Supervision, Project administration, Conceptualization.

Declaration of competing interest

The authors declare that they have no known competing financial interests or personal relationships that could have appeared to influence the work reported in this paper.

Data availability

Data will be made available on request.

Acknowledgments

The authors would like to thank the A.J. Drexel Nanomaterials Institute team, and in particular Dr. Armin VahidMohammadi, for the possibility of executing the general $Ti_3C_2T_x$ characterization and a part of the $Ti_3C_2T_x$ electrochemical characterization at the coin cell level in their laboratories.

Appendix A. Supplementary data

Supplementary data to this article can be found online at https://doi.org/10.1016/j.jpowsour.2024.234287.

References

[1] F. Xia, L.T. Yang, L. Wang, A. Vinel, Internet of Things, Int. J. Commun. Syst. 25 (2012) 1101–1102, https://doi.org/10.1002/dac.2417.
[2] L. Atzori, A. Iera, G. Morabito, The Internet of Things: a survey, comput, Netw 54 (2010) 2787–2805, https://doi.org/10.1016/j.comnet.2010.05.010.
[3] X. Wang, X. Lu, B. Liu, D. Chen, Y. Tong, G. Shen, Flexible energy-storage devices: design consideration and recent progress, Adv. Mater. 26 (2014) 4763–4782, https://doi.org/10.1002/adma.201400910.
[4] K.-H. Choi, D.B. Ahn, S.-Y. Lee, Current status and challenges in printed batteries: toward form factor-free, monolithic integrated power sources, ACS Energy Lett. 3 (2018) 220–236, https://doi.org/10.1021/acsenergylett.7b01086.
[5] A.M. Gaikwad, A.C. Arias, D.A. Steingart, Recent progress on printed flexible batteries: mechanical challenges, printing technologies, and future prospects, Energy Technol. 3 (2015) 305–328, https://doi.org/10.1002/ente.201402182.
[6] L. Kong, C. Tang, H.-J. Peng, J.-Q. Huang, Q. Zhang, Advanced energy materials for flexible batteries in energy storage: a review, SmartMat 1 (2020), https://doi.org/10.1002/smm2.1007.
[7] C.L. Cobb, C.C. Ho, Additive manufacturing: rethinking battery design, Interf. Mag. 25 (2016) 75–78, https://doi.org/10.1149/2.F08161if.
[8] Y. Pang, Y. Cao, Y. Chu, M. Liu, K. Snyder, D. MacKenzie, C. Cao, Additive manufacturing of batteries, Adv. Funct. Mater. 30 (2020) 1906244, https://doi.org/10.1002/adfm.201906244.
[9] M. Gao, L. Li, Y. Song, Inkjet printing wearable electronic devices, J. Mater. Chem. C 5 (2017) 2971–2993, https://doi.org/10.1039/C7TC00038C.
[10] S. Kholghi Eshkalak, A. Chinnappan, W.A.D.M. Jayathilaka, M. Khatibzadeh, E. Kowsari, S. Ramakrishna, A review on inkjet printing of CNT composites for smart applications, Appl. Mater. Today 9 (2017) 372–386, https://doi.org/10.1016/j.apmt.2017.09.003.
[11] K. Wang, S. Luo, Y. Wu, X. He, F. Zhao, J. Wang, K. Jiang, S. Fan, Super-aligned carbon nanotube films as current collectors for lightweight and flexible lithium ion batteries, Adv. Funct. Mater. 23 (2013) 846–853, https://doi.org/10.1002/adfm.201202412.
[12] S.W. Kim, K.Y. Cho, Current collectors for flexible lithium ion batteries: a review of materials, J. Electrochem. Sci. Technol. 6 (2015) 1–6, https://doi.org/10.33961/JECST.2015.6.1.1.
[13] Y. Yue, H. Liang, 3D current collectors for lithium-ion batteries: a topical review, Small Methods 2 (2018) 1800056, https://doi.org/10.1002/smtd.201800056.
[14] P. Zhu, D. Gastol, J. Marshall, R. Sommerville, V. Goodship, E. Kendrick, A review of current collectors for lithium-ion batteries, J. Power Sources 485 (2021) 229321, https://doi.org/10.1016/j.jpowsour.2020.229321.
[15] A. Sumboja, J. Liu, W.G. Zheng, Y. Zong, H. Zhang, Z. Liu, Electrochemical energy storage devices for wearable technology: a rationale for materials selection and cell design, Chem. Soc. Rev. 47 (2018) 5919–5945, https://doi.org/10.1039/C8CS00237A.
[16] L. Li, Z. Wu, S. Yuan, X.-B. Zhang, Advances and challenges for flexible energy storage and conversion devices and systems, Energy Environ. Sci. 7 (2014) 2101, https://doi.org/10.1039/c4ee00318g.
[17] M. Yamada, T. Watanabe, T. Gunji, J. Wu, F. Matsumoto, Review of the design of current collectors for improving the battery performance in lithium-ion and post-lithium-ion batteries, Electrochemistry (Tokyo, Jpn.) 1 (2020) 124–159, https://doi.org/10.3390/electrochem1020011.
[18] M.C. Dang, T.M.D. Dang, E. Fribourg-Blanc, Silver nanoparticles ink synthesis for conductive patterns fabrication using inkjet printing technology, Adv. Nat. Sci. Nanosci. Nanotechnol. 6 (2014) 015003, https://doi.org/10.1088/2043-6262/6/1/015003.
[19] M. Deng, X. Zhang, Z. Zhang, Z. Xin, Y. Song, A gold nanoparticle ink suitable for the fabrication of electrochemical electrode by inkjet printing, J. Nanosci. Nanotechnol. 14 (2014) 5114–5119, https://doi.org/10.1166/jnn.2014.7208.
[20] W. Shen, X. Zhang, Q. Huang, Q. Xu, W. Song, Preparation of solid silver nanoparticles for inkjet printed flexible electronics with high conductivity, Nanoscale 6 (2014) 1622–1628, https://doi.org/10.1039/C3NR05479A.
[21] L. Nayak, S. Mohanty, S.K. Nayak, A. Ramadoss, A review on inkjet printing of nanoparticle inks for flexible electronics, J. Mater. Chem. C 7 (2019) 8771–8795, https://doi.org/10.1039/C9TC01630A.
[22] S. Jang, Y. Seo, J. Choi, T. Kim, J. Cho, S. Kim, D. Kim, Sintering of inkjet printed copper nanoparticles for flexible electronics, Scripta Mater. 62 (2010) 258–261, https://doi.org/10.1016/j.scriptamat.2009.11.011.
[23] J.S. Kang, H.S. Kim, J. Ryu, H. Thomas Hahn, S. Jang, J.W. Joung, Inkjet printed electronics using copper nanoparticle ink, J. Mater. Sci. Mater. Electron. 21 (2010) 1213–1220, https://doi.org/10.1007/s10854-009-0049-3.
[24] S. Magdassi, M. Grouchko, O. Berezin, A. Kamyshny, Triggering the sintering of silver nanoparticles at room temperature, ACS Nano 4 (2010) 1943–1948, https://doi.org/10.1021/nn901868t.
[25] Z. Zhang, X. Zhang, Z. Xin, M. Deng, Y. Wen, Y. Song, Synthesis of monodisperse silver nanoparticles for ink-jet printed flexible electronics, Nanotechnology 22 (2011) 425601, https://doi.org/10.1088/0957-4484/22/42/425601.
[26] Y. Gu, J.F. Federici, Fabrication of a flexible current collector for lithium ion batteries by inkjet printing, Batteries 4 (2018) 42, https://doi.org/10.3390/batteries4030042.
[27] R.P. Tortorich, J.-W. Choi, Inkjet printing of carbon nanotubes, Nanomaterials 3 (2013) 453–468, https://doi.org/10.3390/nano3030453.
[28] E.B. Secor, P.L. Prabhumirashi, K. Puntambekar, M.L. Geier, M.C. Hersam, Inkjet printing of high conductivity, flexible graphene patterns, J. Phys. Chem. Lett. 4 (2013) 1347–1351, https://doi.org/10.1021/jz400644c.
[29] J. Li, F. Ye, S. Vaziri, M. Muhammed, M.C. Lemme, M. Östling, Efficient inkjet printing of graphene, Adv. Mater. 25 (2013) 3985–3992, https://doi.org/10.1002/adma.201300361.
[30] Y. Xu, I. Hennig, D. Freyberg, A. James Strudwick, M. Georg Schwab, T. Weitz, K. Chih-Pei Cha, Inkjet-printed energy storage device using graphene/polyaniline inks, J. Power Sources 248 (2014) 483–488, https://doi.org/10.1016/j.jpowsour.2013.09.096.
[31] K. Kordás, T. Mustonen, G. Tóth, H. Jantunen, M. Lajunen, C. Soldano, S. Talapatra, S. Kar, R. Vajtai, P.M. Ajayan, Inkjet printing of electrically conductive patterns of carbon nanotubes, Small 2 (2006) 1021–1025, https://doi.org/10.1002/smll.200600061.
[32] O.-S. Kwon, H. Kim, H. Ko, J. Lee, B. Lee, C.-H. Jung, J.-H. Choi, K. Shin, Fabrication and characterization of inkjet-printed carbon nanotube electrode patterns on paper, Carbon 58 (2013) 116–127, https://doi.org/10.1016/j.carbon.2013.02.039.

[33] Z. Fan, Y. Wang, Z. Xie, D. Wang, Y. Yuan, H. Kang, B. Su, Z. Cheng, Y. Liu, Modified MXene/holey graphene films for advanced supercapacitor electrodes with superior energy storage, Adv. Sci. 5 (2018) 1800750, https://doi.org/10.1002/advs.201800750.
[34] M. Alhabeb, K. Maleski, B. Anasori, P. Lelyukh, L. Clark, S. Sin, Y. Gogotsi, Guidelines for synthesis and processing of two-dimensional titanium carbide ($Ti_3C_2T_x$ MXene), Chem. Mater. 29 (2017) 7633–7644, https://doi.org/10.1021/acs.chemmater.7b02847.
[35] C. Ferrara, A. Gentile, S. Marchionna, R. Ruffo, $Ti_3C_2T_x$ MXene compounds for electrochemical energy storage, Curr. Opin. Electrochem. 29 (2021) 100764, https://doi.org/10.1016/j.coelec.2021.100764.
[36] T.S. Mathis, K. Maleski, A. Goad, A. Sarycheva, M. Anayee, A.C. Foucher, K. Hantanasirisakul, C.E. Shuck, E.A. Stach, Y. Gogotsi, Modified MAX phase synthesis for environmentally stable and highly conductive Ti_3C_2 MXene, ACS Nano 15 (2021) 6420–6429, https://doi.org/10.1021/acsnano.0c08357.
[37] M. Xin, J. Li, Z. Ma, L. Pan, Y. Shi, MXenes and their applications in wearable sensors, Front. Chem. 8 (2020) 297. https://www.frontiersin.org/article/10.3389/fchem.2020.00297.
[38] D. Wen, X. Wang, L. Liu, C. Hu, C. Sun, Y. Wu, Y. Zhao, J. Zhang, X. Liu, G. Ying, Inkjet printing transparent and conductive MXene ($Ti_3C_2T_x$) films: a strategy for flexible energy storage devices, ACS Appl. Mater. Interfaces 13 (2021) 17766–17780, https://doi.org/10.1021/acsami.1c00724.
[39] S. Uzun, M. Schelling, K. Hantanasirisakul, T.S. Mathis, R. Askeland, G. Dion, Y. Gogotsi, Additive-free aqueous MXene inks for thermal inkjet printing on textiles, Small 17 (2021) 2006376, https://doi.org/10.1002/smll.202006376.
[40] C.-H. Wang, N. Kurra, M. Alhabeb, J.-K. Chang, H.N. Alshareef, Y. Gogotsi, Titanium carbide (MXene) as a current collector for lithium-ion batteries, ACS Omega 3 (2018) 12489–12494, https://doi.org/10.1021/acsomega.8b02032.
[41] P. Viviani, E. Gibertini, F. Iervolino, M. Levi, L. Magagnin, Carbon additive effect on the electrochemical performances of inkjet printed thin-film $Li_4Ti_5O_{12}$ electrodes, J. Manuf. Process. 72 (2021) 411–418, https://doi.org/10.1016/j.jmapro.2021.10.039.
[42] X. Wu, K. Song, X. Zhang, N. Hu, L. Li, W. Li, L. Zhang, H. Zhang, Safety issues in lithium ion batteries: materials and cell design, Front. Energy Res. 7 (2019) 65. https://www.frontiersin.org/articles/10.3389/fenrg.2019.00065.
[43] M. Shekhirev, C.E. Shuck, A. Sarycheva, Y. Gogotsi, Characterization of MXenes at every step, from their precursors to single flakes and assembled films, Prog. Mater. Sci. 120 (2021) 100757, https://doi.org/10.1016/j.pmatsci.2020.100757.
[44] A. Zhou, C.-A. Wang, Y. Hunag, Synthesis and mechanical properties of Ti_3AlC_2 by spark plasma sintering, J. Mater. Sci. 38 (2003) 3111–3115, https://doi.org/10.1023/A:1024777213910.
[45] A.S. Zeraati, S.A. Mirkhani, P. Sun, M. Naguib, P.V. Braun, U. Sundararaj, Improved synthesis of $Ti_3C_2T_x$ MXenes resulting in exceptional electrical conductivity, high synthesis yield, and enhanced capacitance, Nanoscale 13 (2021) 3572–3580, https://doi.org/10.1039/D0NR06671K.
[46] C.E. Shuck, A. Sarycheva, M. Anayee, A. Levitt, Y. Zhu, S. Uzun, V. Balitskiy, V. Zahorodna, O. Gogotsi, Y. Gogotsi, Scalable synthesis of $Ti_3C_2T_x$ MXene, Adv. Eng. Mater. 22 (2020) 1901241, https://doi.org/10.1002/adem.201901241.
[47] K. Maleski, C.E. Ren, M.-Q. Zhao, B. Anasori, Y. Gogotsi, Size-dependent physical and electrochemical properties of two-dimensional MXene flakes, ACS Appl. Mater. Interfaces 10 (2018) 24491–24498, https://doi.org/10.1021/acsami.8b04662.
[48] M. Alhabeb, K. Maleski, B. Anasori, P. Lelyukh, L. Clark, S. Sin, Y. Gogotsi, Guidelines for synthesis and processing of two-dimensional titanium carbide ($Ti_3C_2T_x$ MXene), Chem. Mater. 29 (2017) 7633–7644, https://doi.org/10.1021/acs.chemmater.7b02847.
[49] S. Seyedin, J. Zhang, K.A.S. Usman, S. Qin, A.M. Glushenkov, E.R.S. Yanza, R. T. Jones, J.M. Razal, Facile solution processing of stable MXene dispersions towards conductive composite fibers, Glob. Chall. 3 (2019) 1900037, https://doi.org/10.1002/gch2.201900037.
[50] J. Ma, S. Zheng, Y. Cao, Y. Zhu, P. Das, H. Wang, Y. Liu, J. Wang, L. Chi, S. (Frank) Liu, Z.-S. Wu, Aqueous MXene/PH1000 hybrid inks for inkjet-printing micro-supercapacitors with unprecedented volumetric capacitance and modular self-powered microelectronics, Adv. Energy Mater. 11 (2021) 2100746, https://doi.org/10.1002/aenm.202100746.
[51] C.J. Zhang, L. McKeon, M.P. Kremer, S.-H. Park, O. Ronan, A. Seral-Ascaso, S. Barwich, C.Ó. Coileáin, N. McEvoy, H.C. Nerl, B. Anasori, J.N. Coleman, Y. Gogotsi, V. Nicolosi, Additive-free MXene inks and direct printing of micro-supercapacitors, Nat. Commun. 10 (2019) 1795, https://doi.org/10.1038/s41467-019-09398-1.
[52] J. Zhang, N. Kong, S. Uzun, A. Levitt, S. Seyedin, P.A. Lynch, S. Qin, M. Han, W. Yang, J. Liu, X. Wang, Y. Gogotsi, J.M. Razal, Scalable manufacturing of free-standing, strong $Ti_3C_2T_x$ MXene films with outstanding conductivity, Adv. Mater. 32 (2020) 2001093, https://doi.org/10.1002/adma.202001093.
[53] M. Lotya, A. Rakovich, J.F. Donegan, J.N. Coleman, Measuring the lateral size of liquid-exfoliated nanosheets with dynamic light scattering, Nanotechnology 24 (2013) 265703, https://doi.org/10.1088/0957-4484/24/26/265703.
[54] T. Wu, P.R.C. Kent, Y. Gogotsi, D. Jiang, How water attacks MXene, Chem. Mater. 34 (2022) 4975–4982, https://doi.org/10.1021/acs.chemmater.2c00224.
[55] Y. Son, H. Cha, C. Jo, A.S. Groombridge, T. Lee, A. Boies, J. Cho, M. De Volder, Reliable protocols for calculating the specific energy and energy density of Li-Ion batteries, Mater. Today Energy 21 (2021) 100838, https://doi.org/10.1016/j.mtener.2021.100838.
[56] C.-S. Kim, K.M. Jeong, K. Kim, C.-W. Yi, Effects of capacity ratios between anode and cathode on electrochemical properties for lithium polymer batteries, Electrochim. Acta 155 (2015) 431–436, https://doi.org/10.1016/j.electacta.2014.12.005.
[57] C. Liu, K. Qian, D. Lei, B. Li, F. Kang, Y.-B. He, Deterioration mechanism of $LiNi_{0.8}Co_{0.15}Al_{0.05}O_2$/graphite–$SiO_x$ power batteries under high temperature and discharge cycling conditions, J. Mater. Chem. A 6 (2018) 65–72, https://doi.org/10.1039/C7TA08703A.